


Cite this: *Nanoscale Adv.*, 2019, **1**, 2009

# Highly sensitive and room temperature detection of ultra-low concentrations of O<sub>3</sub> using self-powered sensing elements of Cu<sub>2</sub>O nanocubes

E. Petromichelaki,<sup>a</sup> E. Gagaoudakis,<sup>ab</sup> K. Moschovis,<sup>a</sup> L. Tsetseris,<sup>id c</sup>  
T. D. Anthopoulos,<sup>id d</sup> G. Kiriakidis<sup>ab</sup> and V. Binas<sup>id \*ab</sup>

The fundamental development of the design of novel self-powered ozone sensing elements, operating at room temperature, based on p-type metal oxides paves the way to a new class of low cost, highly promising gas sensing devices. In this work, p-type Cu<sub>2</sub>O nanocubes were synthesized by a simple solution-based method and tested as a self-powered ozone sensing element, at room temperature (25 °C) for the first time. Highly crystalline Cu<sub>2</sub>O nanocubes with 30 nm size were characterized by X-ray Diffraction (XRD), Scanning Electron Microscopy (SEM) and Transmission Electron Microscopy (TEM). Self-powered sensing elements of Cu<sub>2</sub>O nanocubes have been successfully fabricated by deposition of Cu<sub>2</sub>O nanocubes on interdigitated electrodes (IDEs) consisting of two connection tracks with 500 digits and a gap of 5 μm in order to investigate their response to ozone at room temperature. The experimental results showed that the use of nanocubes as sensing elements was suitable for detecting ultra-low concentrations of O<sub>3</sub> down to 10 ppb at room temperature with very high sensitivity (28%) and a very low response/recovery time. The reversible sensing process of the relatively weak binding of O<sub>3</sub> species by trapping sites on Cu<sub>2</sub>O facets with increased oxygen content was studied by using density functional theory (DFT) calculations.

Received 23rd January 2019  
Accepted 3rd April 2019

DOI: 10.1039/c9na00043g

rsc.li/nanoscale-advances

## Introduction

Some of the most common pollutant gases in air are NO<sub>2</sub>, O<sub>3</sub>, CO, SO<sub>2</sub> and NO. Among them, ozone (O<sub>3</sub>) is closely related to human life since it is widely used in a numerous applications such as in food storage and in the pharmaceutical, textile and chemical industries. Moreover, it works as a protective layer in the Earth's stratosphere for human health, absorbing the harmful ultraviolet (UV) radiation. On the other hand, according to the World Health Organization (WHO), excess exposure to ozone concentrations of more than 1 parts per million (ppm) can cause breathing problems, trigger asthma, reduce lung function and induce lung diseases and induce the burning eyes symptom. Thus, it is apparent that detection of ozone at ultra-low concentrations (*i.e.* low ppb levels) is of great importance.<sup>1</sup>

The use of metal oxide semiconductors as sensing elements for monitoring air quality has emerged as a low cost alternative

due to fast response/recovery rates and low detection limits.<sup>2–4</sup> In particular, cuprous oxide (Cu<sub>2</sub>O) as a p-type semiconductor, with a narrow direct energy band gap of  $E_g = 2.17$  eV, has been tested as gas sensor material in recent years and highlighted due to its good stability and high conductivity. In addition, Cu<sub>2</sub>O is non-toxic and copper is earth abundant and hence inexpensive. To date, numerous micro- and nano-structures of octahedral<sup>4,5</sup> and polyhedral<sup>6</sup> Cu<sub>2</sub>O have been reported, with a variety of morphologies, such as nanocubes,<sup>7,8</sup> spheres,<sup>9</sup> nanowires,<sup>10</sup> and quasi-spherical shapes,<sup>11</sup> using solution-based synthetic methods. Cu<sub>2</sub>O films have been also been produced *via* a variety of methods including thermal oxidation, magnetron sputtering, spray pyrolysis, *etc.*<sup>12–15</sup> In the field of gas-sensing, Cu<sub>2</sub>O has great potential in detecting various pollutants in their gaseous form, due to its significant surface reactivity with both reducing (ethanol, gasoline, CO, and H<sub>2</sub>S)<sup>3,5,7,8,16</sup> and oxidizing gases (NO<sub>2</sub>, CO<sub>2</sub>, CH<sub>4</sub>, and O<sub>3</sub>).<sup>4,6,7,9,10,17,18</sup> However, the working temperature of the sensors fabricated using Cu<sub>2</sub>O is significantly higher than room temperature (25 °C).<sup>4,6,9–13</sup>

Considering the detection of O<sub>3</sub>, the majority of studies are related to composites with other metals such as CuAlO<sub>2</sub> and CuCrO<sub>2</sub> tested against a variety of gas concentrations and at different working temperatures. To the best of our knowledge, Ouali *et al.* were the only report on the use of Cu<sub>2</sub>O for 10 to 1000 ppb level sensing of O<sub>3</sub> at an operating temperature of 175 °C.<sup>17</sup> Moreover, Zhou *et al.* synthesized both nanocrystals

<sup>a</sup>Institute of Electronic Structure and Laser (IESL), FORTH, P. O. Box 1527, Vasilika Vouton, GR-71110 Heraklion, Greece. E-mail: binasbill@iesl.forth.gr

<sup>b</sup>Crete Center for Quantum Complexity & Nanotechnology (CCQCN), Department of Physics, University of Crete, GR-71003, Heraklion, Greece

<sup>c</sup>Department of Physics, National Technical University of Athens, GR-15780 Athens, Greece

<sup>d</sup>Physical Science and Engineering Division, King Abdullah University of Science and Technology, Saudi Arabia


(10–80 nm) and thin films of  $\text{CuCrO}_2$  for the detection of 50–200 ppm  $\text{O}_3$  at room temperature (25 °C), with the maximum response (6%) measured at 200 ppm.<sup>18</sup> Deng *et al.* prepared  $\text{CuCrO}_2$  thin films for the detection of 100 ppb  $\text{O}_3$  at room temperature, using air for the recovery of the system.<sup>19</sup> Zheng *et al.* prepared transparent  $\text{CuAlO}_2$  thin films for the detection of 0.1%  $\text{O}_3$  (99.9%  $\text{O}_2$ ) at room temperature,<sup>20</sup> while Thirumalairajan *et al.* synthesized  $\text{CuAlO}_2$  nanostructures of two different sizes (40 and 80 nm) with flower-like and hexagonal morphologies, for the sensing of 200, 600, and 1150 ppb  $\text{O}_3$  at 250 °C, with the best response and recovery time of 25 and 39 s for 200 ppb.<sup>21</sup> Finally, Baratto *et al.* used  $\text{CuAlO}_2$  thin films for the detection of a wide range of  $\text{O}_3$  concentrations (70–350 ppb) at an operating temperature between 300 °C and 500 °C in a humid air background<sup>22</sup> and Thirumalairajan *et al.* synthesized  $\text{CuAlO}_2$  microspheres to detect 200, 600, and 1150 ppb  $\text{O}_3$  at 200 °C, with the response and recovery times being equal to 29 s and 45 s (for 200 ppb at 200 °C), respectively, and the highest response reaching the value of 2.8 at 1150 ppb.<sup>23</sup>

In this work, we describe a one pot, controllable synthesis of p-type  $\text{Cu}_2\text{O}$  nanocubes with approximately 30 nm size, through an additive-free aqueous solution route, at room temperature. The method is facile, fast, eco-friendly and inexpensive. Highly crystalline  $\text{Cu}_2\text{O}$  nanocubes were deposited on interdigitated electrodes for gas sensing measurements. Two-terminal direct current–voltage measurements showed that the use of the nanocubes as the sensing element was suitable for detecting ultra-low concentrations of  $\text{O}_3$  down to 10 ppb at room temperature (25 °C) with high sensitivity (28%) and low response/recovery times. The reversible sensing process of the relatively weak binding of  $\text{O}_3$  species by trapping sites on  $\text{Cu}_2\text{O}$  facets with increased oxygen content was calculated by employing density functional theory (DFT). This is the first report on the use of  $\text{Cu}_2\text{O}$  nanocubes for the detection of ultra-low  $\text{O}_3$  concentrations, at room temperature, highlighting the tremendous potential of this rather simple technology.

## Experimental section

Copper(II) acetate hydrate ( $\text{Cu}(\text{CH}_3\text{CO}_2)_2 \cdot x\text{H}_2\text{O}$ , 98%), sodium hydroxide (NaOH, 98–100.5%) and L-ascorbic acid ( $\text{C}_6\text{H}_8\text{O}_6$ , 99%) used in this work were obtained from Sigma-Aldrich. All the reagents were used as received without any further purification.

### Synthetic procedure of $\text{Cu}_2\text{O}$ nanocubes

In a typical synthesis, a mixture of 40.0 mL of 0.009 M L-ascorbic acid solution and 64.0 mL of 0.1 M NaOH solution was added to 64.0 mL of previously prepared 0.005 M copper(II) acetate ( $\text{Cu}(\text{Ac})_2$ ) solution under stirring. The mixed solution was then stirred vigorously for 15 min, during which the solution became yellow and turbid, indicating the formation of  $\text{Cu}_2\text{O}$ . Finally, the precipitates were collected through centrifugation and washed with distilled water and absolute ethanol several times. All the experiments were carried out at room temperature.

### Materials characterization

The crystallographic structure of  $\text{Cu}_2\text{O}$  was demonstrated by X-ray diffraction (XRD) measurements using a Rigaku RINT-2000 system with  $\text{Cu K}\alpha$  ( $\lambda = 1.5418 \text{ \AA}$ ) X-rays produced at 40 kV and 82 mA. The  $2\theta$  collection range was 10–80° with a scan rate of  $0.05^\circ \text{ s}^{-1}$ . The average crystal size ( $D$  in nm) of nanoparticles was calculated from the line broadening of the X-ray diffraction peak according to the following Scherrer's formula:

$$D = k\lambda/\beta \cos \theta, \quad (1)$$

where  $k$  is the Scherrer constant ( $\sim 0.9$ ),  $\lambda$  is the wavelength of the X-ray radiation ( $1.54 \text{ \AA}$  for  $\text{CuK}\alpha$ ),  $\beta$  is the full width at half maximum (FWHM) of the diffraction peak measured at  $2\theta$ , and  $\theta$  is the Bragg angle. The surface morphology and microstructure analysis was performed by both Field Emission Scanning Electron Microscopy (JEOL 7000) at an acceleration voltage of 15 kV and Transmission Electron Microscopy (TEM) using a JEM-2100 instrument equipped with LaB6 filament, operating at 200 kV.

### Gas sensor fabrication and measurements of ozone sensing properties

A paste of  $\text{Cu}_2\text{O}$  nanoparticles was prepared by dispersing 4.0 mg of  $\text{Cu}_2\text{O}$  nanocubes in 1 mL of methanol. Subsequently, the paste was drop-cast onto pre-patterned interdigitated (IDT) Pt electrodes on a glass substrate and left to dry at room temperature, resulting to the formation of a thin layer. The interdigitated electrodes were composed of two connection (all made of platinum on a glass substrate) tracks with 500 digits and a gap of  $5 \mu\text{m}$  to ensure a good coverage of the  $\text{Cu}_2\text{O}$  nanocubes. Moreover, they are compatible with CMOS technology and able to operate at room temperature allowing low power consumption. The as-prepared devices were used for the ozone sensing measurements, inside a purpose-built gas test chamber (Fig. 1). The ozone was obtained using a calibrated ozone generator equipped with an internal analyzer (Thermo Electron Corporation, model 49i) at different concentrations in the range 10 to 820 ppb, while for the recovery of the sensor the chamber was backfilled with ambient air. Electrical characterization of the devices as a function of ozone concentration was performed by monitoring the electrical current level at a constant bias voltage of 10 V, using a Keithley 6517A electrometer. All the sensing measurements were carried out at room temperature. The sensitivity of the sensor is defined as

$$S (\%) = [(I_{\text{gas}} - I_{\text{air}})/I_{\text{air}}] \times 100\%, \quad (2)$$

where  $I_{\text{air}}$  denotes the current value before gas injection, while  $I_{\text{gas}}$  denotes the maximum current value in the presence of ozone. The response time of the sensor is defined as the time required for a change in the current to reach 90% of the initial value when exposed to a set ozone gas concentration. Similarly, the time required for the current of the sensor to reach 90% of the initial value after the ozone gas has been turned off is defined as the recovery time.



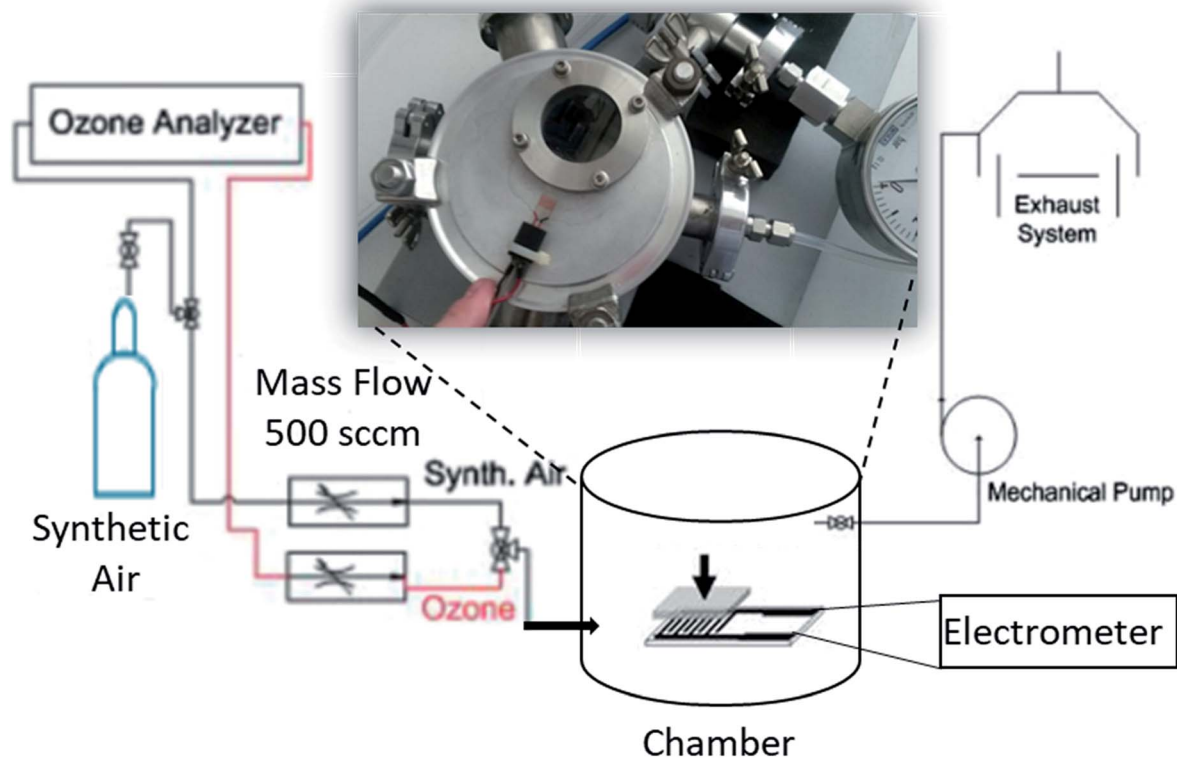


Fig. 1 Conductivity-based system with a gas test chamber.

### Density functional theory (DFT) calculations

First-principles spin-polarized calculations were performed with the Density Functional Theory (DFT) code Quantum Espresso,<sup>24</sup> projector-augmented waves<sup>25</sup> to model the interactions between valence electrons and ionic cores, the PW91 exchange–correlation (xc) functional<sup>26</sup> and the DFT-D2 method<sup>27</sup> to take into account van der Waals interactions. The energy cutoff of the plane wave basis was set at 75 Rydberg (Ry) and integrations in reciprocal space used  $2 \times 2 \times 1$  or  $4 \times 4 \times 1$  Monkhorst–Pack  $k$ -point grids<sup>28</sup> or tetrahedron sampling,<sup>29</sup> respectively, for the determination of total energies or electronic densities of states. The (001) surfaces of  $\text{Cu}_2\text{O}$  were modeled as slabs with 7 layers and  $2 \times 2$  supercells in the lateral directions (with at least 86 atoms). The relaxation of structures was terminated when the energy converged within 10–6 Ry. We also obtained the energies for the highest occupied (HOMO) and lowest unoccupied (LUMO) molecular orbitals of an  $\text{O}_3$  molecule with the hybrid B3LYP xc-functional<sup>32</sup> and the 6-311+G\* Gaussian basis set (as implemented<sup>30</sup> in the NWChem code).

## Results and discussion

$\text{Cu}_2\text{O}$  nanocubes were characterized using a powder X-ray diffractometer (XRD). Fig. 2a shows the XRD pattern of  $\text{Cu}_2\text{O}$  nanocubes and the standard  $\text{Cu}_2\text{O}$  card. All the diffraction peaks are consistent with the standard card (JCPDS card no. 05-0667) of cubic phase  $\text{Cu}_2\text{O}$  attributed to the (110), (111), (200), (220), (311) and (222) crystal planes. Specifically, the strong and

sharp peaks indicate that the obtained  $\text{Cu}_2\text{O}$  nanocubes are highly crystalline with an average crystal size of 19.7 nm, as calculated using Scherrer's formula. After the controllable synthesis of  $\text{Cu}_2\text{O}$  nanocubes, the representative morphology and size were determined by field emission scanning electron microscopy (FESEM) and high resolution transition electron microscopy (TEM) as shown in Fig. 2b and c. From this, it can be seen that  $\text{Cu}_2\text{O}$  material is mainly composed of uniform cubes that are 30 to 35 nm in size. Highly crystalline  $\text{Cu}_2\text{O}$  nanocubes with 30 nm size were deposited on interdigitated electrodes with a good coverage as shown in Fig. 3a and b.

The two-terminal interdigitated sensor devices were tested at room temperature whilst been exposed to different concentrations of ozone in the range 10–820 ppb. The repeatability of the sensing response was also examined by repeating the measurement several times using different  $\text{Cu}_2\text{O}$  nanocube-based devices. Fig. 4 shows the evolution of the current (measured at a constant bias of 10 volts) as a function of time and exposure to different ozone concentrations. In particular, the measurement included two steps: (i) the sensor was exposed to an atmosphere containing  $\text{O}_3$  with a predetermined concentration for approximately 2 min while the current was monitored in real time; (ii) the ozone flow was turned-off and the device was exposed to ambient air (relative humidity  $\approx$  55%) for approximately 1 min. The same measuring cycle was repeated for  $\text{O}_3$  concentrations of 170, 490 and 820 ppb (Fig. 4). It is clearly evident that the current across the  $\text{Cu}_2\text{O}$  nanocube channel increases in the presence of ozone, an observation





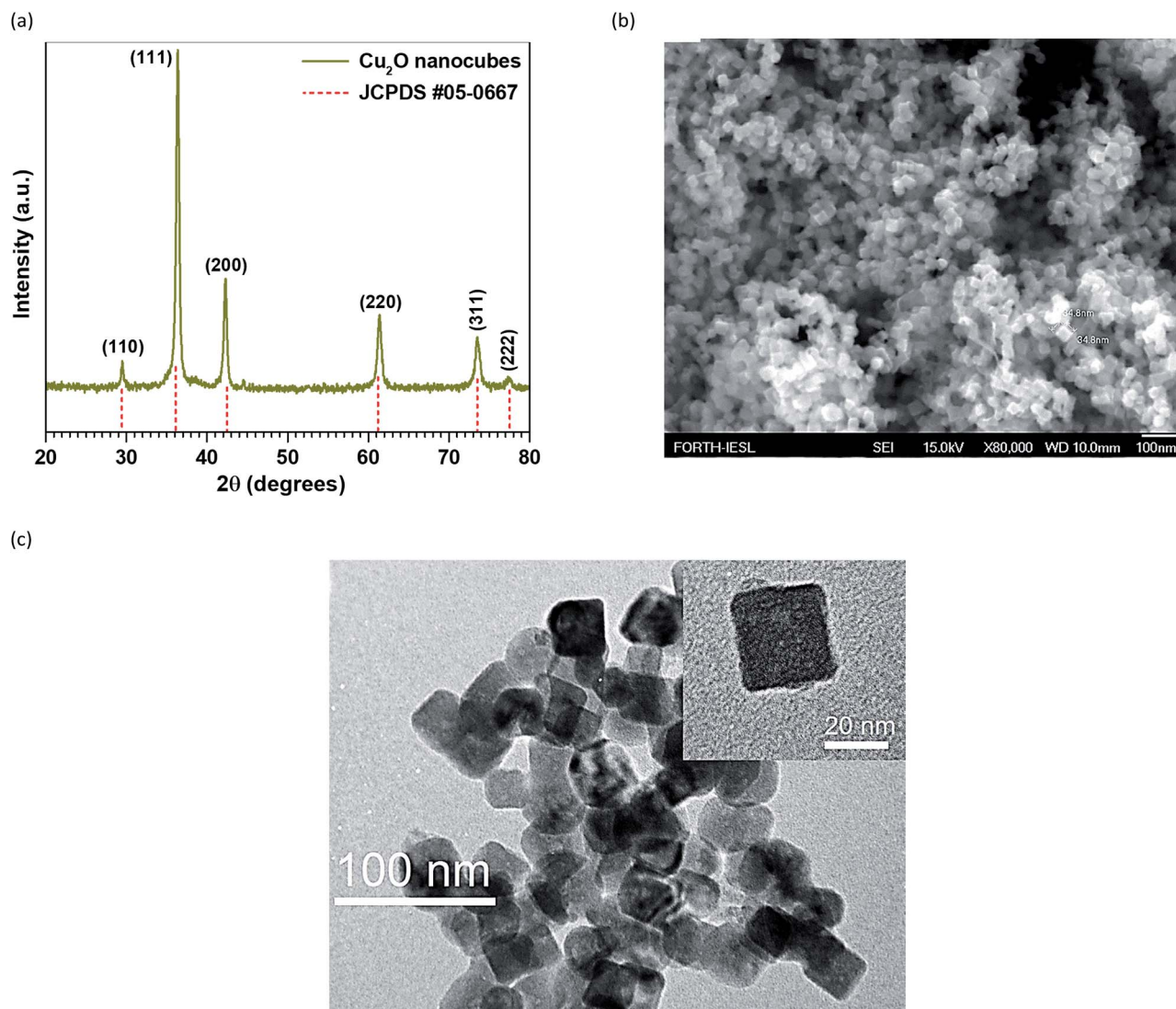


Fig. 2 (a) X-ray diffraction (XRD) pattern of Cu<sub>2</sub>O nanocubes and standard Cu<sub>2</sub>O card. (b and c) FESEM images and TEM images of Cu<sub>2</sub>O nanocubes.

consistent with the p-type conductivity in Cu<sub>2</sub>O nanocubes since an oxidizing gas such as ozone was expected to remove electrons from the top of the valence band of the semiconductor leading to an increased concentration of holes<sup>21</sup> – a process that is discussed in details below. Once the ozone flow is turned off and ambient air is re-injected into the test chamber, the current of the Cu<sub>2</sub>O nanocube channel reduces to almost its original value of  $\approx 0.525 \mu\text{A}$  (see the current level following exposure to 10 ppb ozone). Although, exposure of the sensor to higher ozone concentrations lead to significantly higher current, the latter does not appear to return to its original value following exposure to ambient air for approximately 1 min. This can be attributed to a residual oxidation caused by the amount of ozone.

It is clear from the data shown in Fig. 5a that as the O<sub>3</sub> concentration increases from 10 to 490 ppb both response (30 s) and recovery times (18 s) of the sensor remain stable, with the only exception being the O<sub>3</sub> concentration of 820 ppb where the

response time decreased to 24 s and the recovery time increased to 24 s. The gas sensitivity of the sensor as a function of ozone concentration at room temperature is shown in Fig. 5b, from which it can be seen that it is decreased by increasing O<sub>3</sub> analytic concentration. The reason for this might be the low working temperature (*i.e.* 25 °C), compared with previous studies in which a  $T_{\text{work}}$  of 175 °C was employed.<sup>17</sup> More specifically, this is the first report on the use of Cu<sub>2</sub>O nanocubes as a self-powered sensing element for the detection of ultra-low O<sub>3</sub> concentrations down to 10 ppb with the highest response value of 28% and a response/recovery time of 30/18 s, respectively, at room temperature.

The experimental data presented so far suggest that O<sub>3</sub> species interact with the Cu<sub>2</sub>O nanocrystals, while this interaction allows the whole process to follow in time the periodic supply of ozone molecules to the sample. In order to elucidate possible atomic-scale mechanisms that underlie the key experimental findings, we performed extensive DFT calculations on



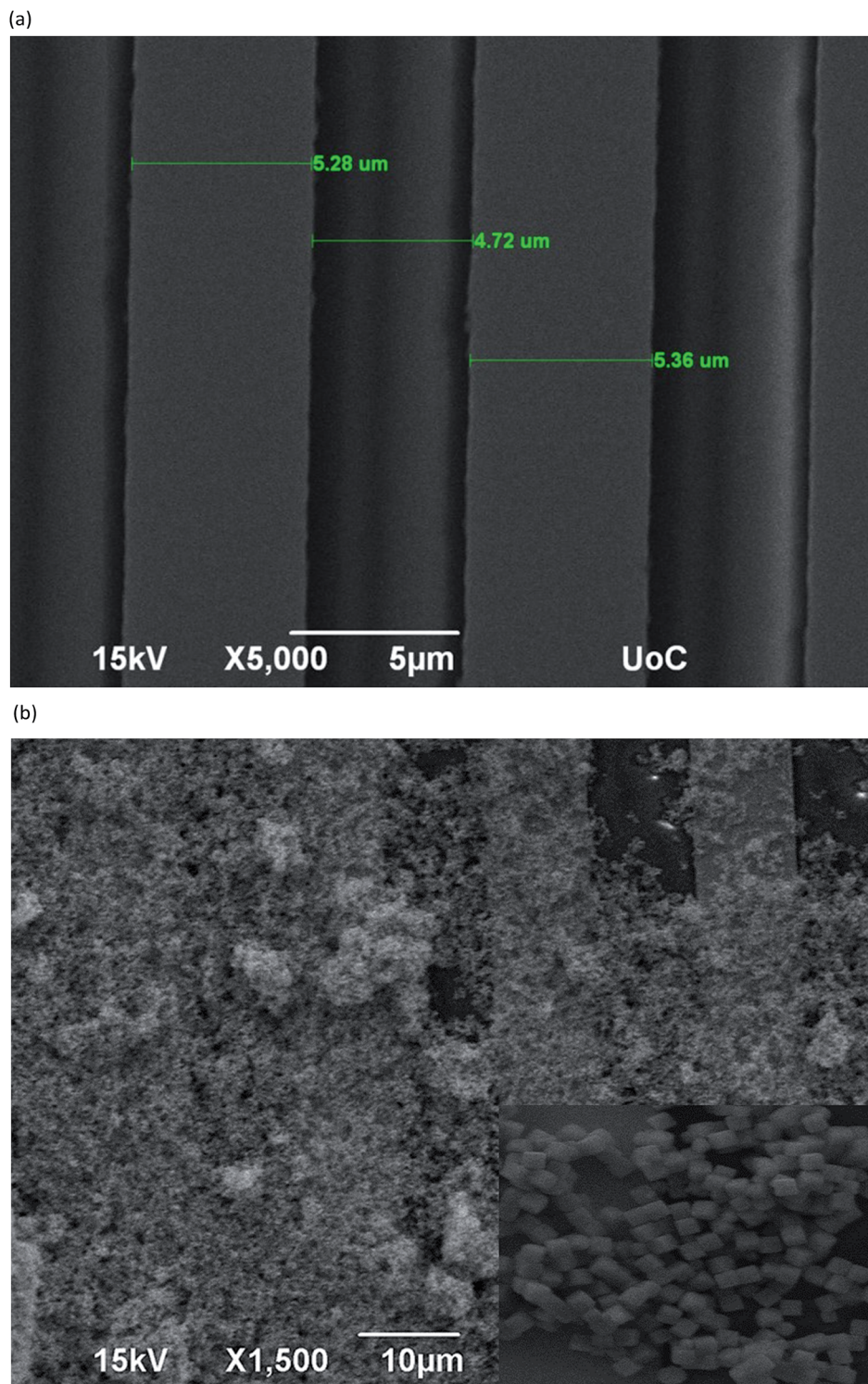


Fig. 3 (a) SEM images of the IDEs with a gap of 5  $\mu\text{m}$ . (b) SEM of coated IDEs and zoomed view of the coated IDEs with nanocubes in the inset.

the adsorption of  $\text{O}_2$  and  $\text{O}_3$  molecules on (001) surfaces, given that (001) facets dominate  $\text{Cu}_2\text{O}$  nanocubes,<sup>8</sup> while (110) and (111) terminations appear, respectively, only as truncated edges and corners.<sup>33</sup>

First, we should note that the calculated LUMO value ( $-5.65$  eV) is lower than the measured<sup>31</sup> valence band maximum ( $-5.3$

eV) of  $\text{Cu}_2\text{O}$ . Hence, any physisorbed  $\text{O}_3$  species should act as electron acceptors for  $\text{Cu}_2\text{O}$ . By the same token, ozone molecules can interact directly with the  $\text{Cu}_2\text{O}$  facets. We found that when these facets have low oxygen content (close to the value associated with the stoichiometry of  $\text{Cu}_2\text{O}$ ),  $\text{O}_2$  and  $\text{O}_3$  molecules chemisorb to configurations with large binding energies





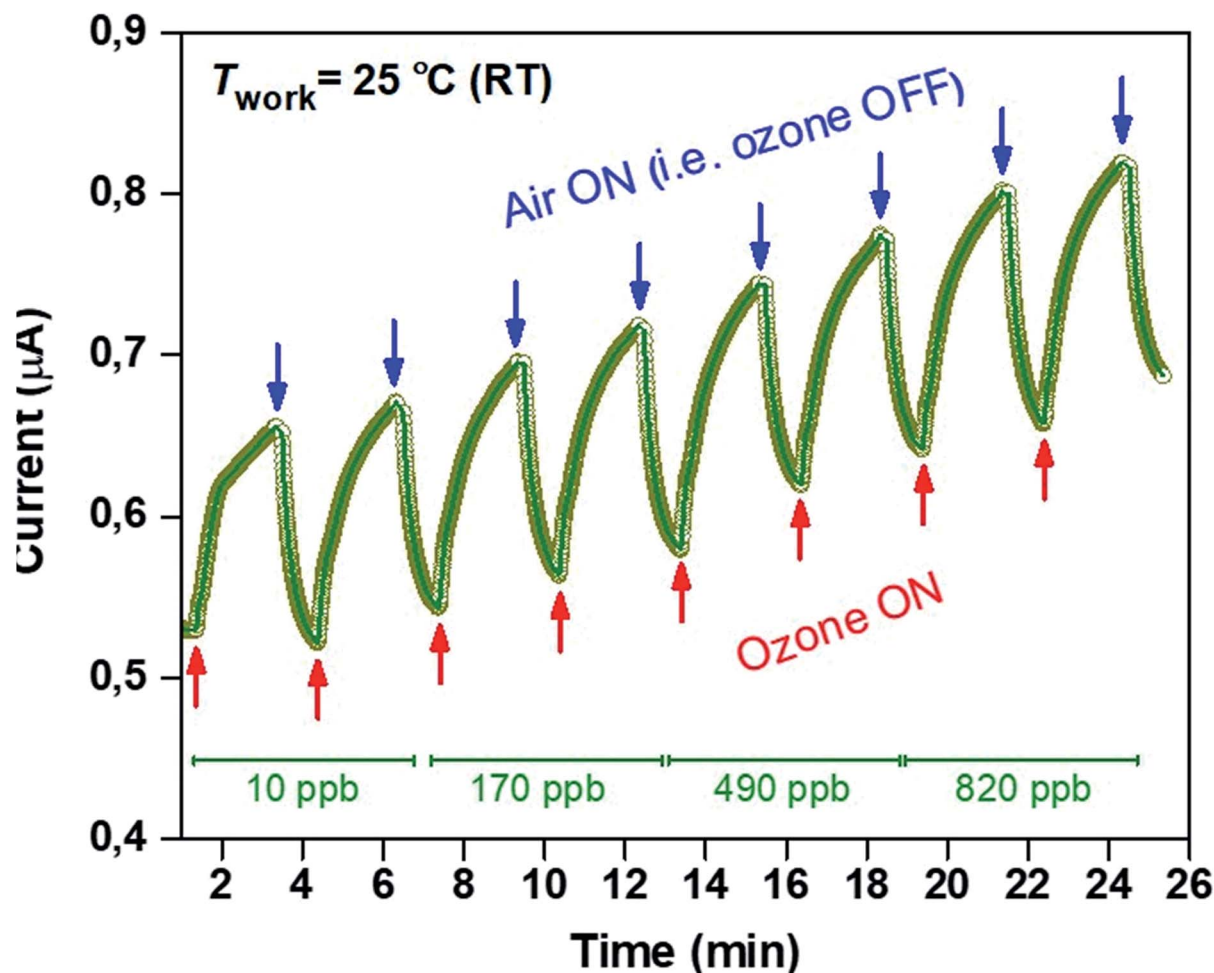


Fig. 4 Current changes at room temperature of  $\text{Cu}_2\text{O}$  nanocubes due to successive increases in  $\text{O}_3$  concentrations.

(in excess of 1.5 eV) and some of the deposited O species move to subsurface sites. Concurrently the Fermi level of the system moves inside its valence band consistent with p-type doping. These results are in agreement with the findings reported by Ouali *et al.*<sup>17</sup>

Fig. 6 shows typical steps for the oxidation reactions taking place on  $\text{Cu}_2\text{O}$  surfaces with a relatively low O content. First,  $\text{O}_2$  molecules chemisorb in barrier-less processes and create species like the one shown in the configuration labelled (a) in Fig. 6. Starting from such a chemisorbed configuration, the adsorbed molecule easily breaks into two O adatoms, since the corresponding barrier is only about 0.4 eV. This low activation energy shows that the process takes place even at room temperature. Following the breakup of the molecule, the two O adatoms relax to the intermediate configuration (c) of Fig. 6, and eventually to an even more stable (by about 2 eV) freshly oxidized structure (not shown here). The oxidation reactions with an  $\text{O}_3$  molecule follow similar steps, namely there is a barrier-less initial chemisorption, followed by an essentially barrier-less breakup of one of the three O atoms of the adsorbed  $\text{O}_3$  species, and then by reactions akin to those depicted in Fig. 6.

On the other hand,  $\text{O}_3$  chemisorption continues to take place on areas with increased oxygen content, but in selected such

cases, the result is the formation of  $\text{O}_3$ -related defects with relatively low binding energies. Fig. 7 shows two such configurations, an  $\text{O}_3$ -protrusion in Fig. 7a with a single Cu–O bond and an inter-Cu  $\text{O}_3$ -bridge in Fig. 7b. The low binding energies of these  $\text{O}_3$  configurations (0.90 eV and 0.40 eV, respectively) suggest that when the ozone supply is interrupted, some of the adsorbed  $\text{O}_3$  species can be replaced by physisorbed  $\text{O}_2$  molecules which are present in much larger numbers and have corresponding binding energies of 0.23 eV and 0.10 eV. With respect to electronic properties, the results of projected DOS (not shown here) show that the defects shown in Fig. 7 introduce peaks at 0.05 eV and 0.3 eV above the Fermi level of the structure, and hence they can indeed play the role of electron acceptors (though we should note that the thickness of the slab and the use of the PW91 xc-functional do not allow us to draw final conclusions on the exact position of these peaks).

The main picture that emerges from these calculations is the following. If  $\text{Cu}_2\text{O}$  nanocrystals are not O-rich in the beginning, then the deposition of electronegative oxygen atoms (through, e.g., the dissociation of  $\text{O}_3$  molecules) contributes to the p-doping of the material. Taking into account also the experimental findings on enhanced hole conductivity, the main reactions during this first stage can be described schematically as:



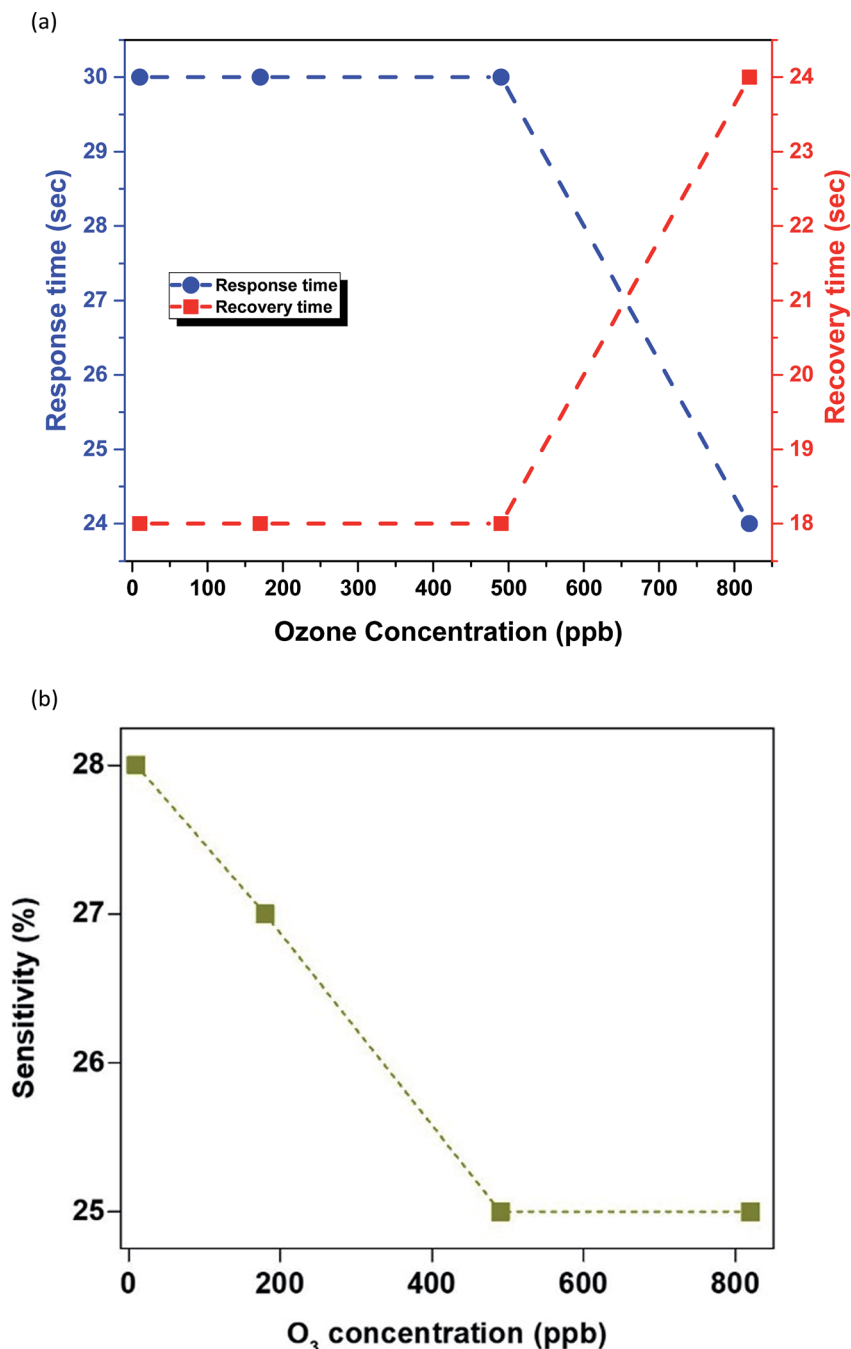
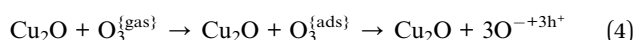
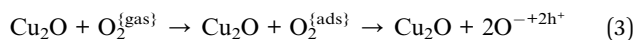
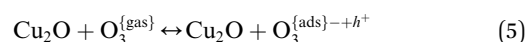


Fig. 5 (a) Response and recovery time (s) of the sensor at different ozone concentrations. (b) Sensing sensitivity as a function of ozone concentration.



When the nanocrystal facets are sufficiently oxidized (a condition which is plausible, but which also depends on the details of growth and operation), then they can selectively trap O<sub>3</sub> molecules with binding energies that are neither very large (so that the process may still be reversible) nor very small (so that it can lead to sensing of even small amounts of ozone). This second stage can be described as:



This atomic-scale picture is consistent with the broad features observed in the experiments. Nevertheless, we should stress that the high reactivity of the material (which also results in large local distortions upon oxygen uptake) leaves open the possibility that other adsorption mechanisms may also be important here. Future studies will explore, for example, the role of humidity or of surface reconstructions.



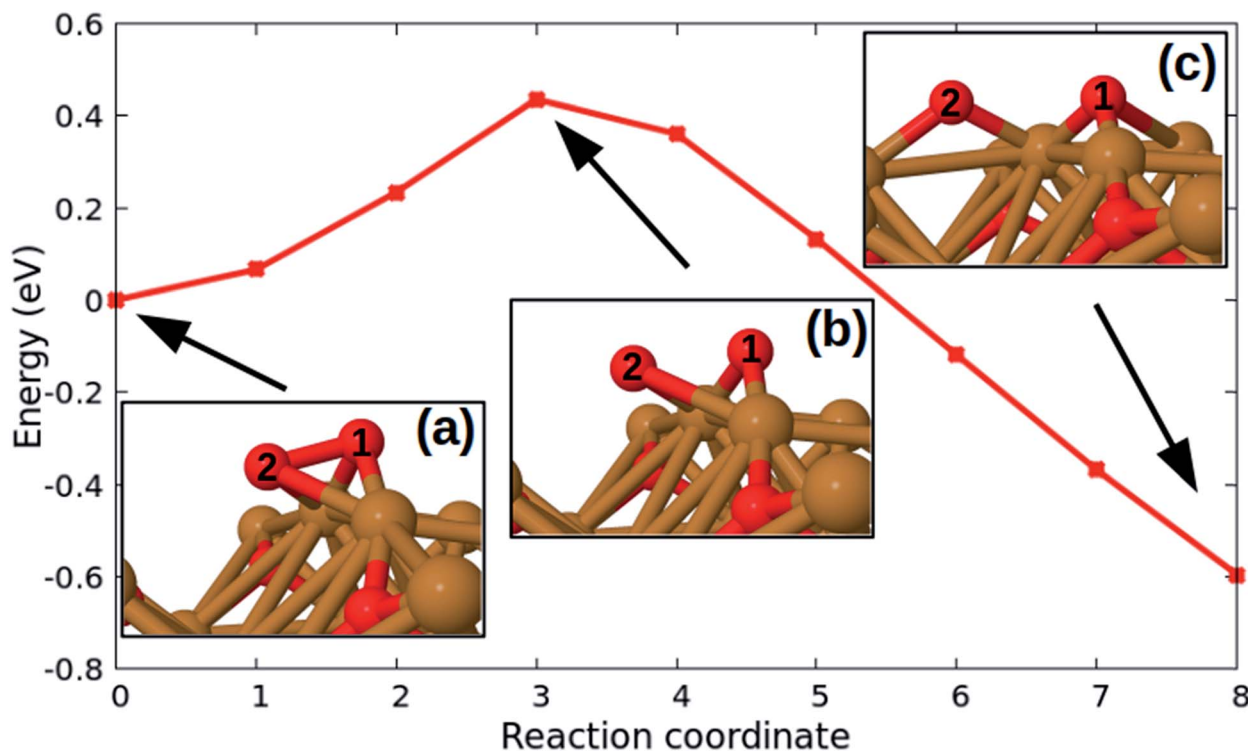


Fig. 6 Energy variation during a typical oxidation reaction on a (001)  $\text{Cu}_2\text{O}$  surface. An  $\text{O}_2$  molecule (its atoms are numbered 1 and 2) chemisorbs with a zero barrier to configuration (a), followed by its breakup to atomic O adatoms and structures (b) and (c). The transition state of the reaction is (b) and the barrier is low and equal to 0.43 eV.

On the basis of the results and analysis presented so far one can argue that there are a few plausible reasons responsible for the fact that the current does not fully recover upon re-exposure of the sensor to ambient air (Fig. 4). The first reason is that the amount of air inserted into chamber for the given recovery (reset) period ( $\sim 1$  min) is not enough to completely decrease the number of holes that are being created by the adsorption of  $\text{O}_3$  on  $\text{Cu}_2\text{O}$  during the

exposure time. Increasing the recovery period would therefore help to reduce the current closer to its original value. Another reason for the incomplete current recovery is dissociation kinetics associated with  $\text{O}_3$  desorption from the surface of  $\text{Cu}_2\text{O}$  at room temperature. This issue could potentially be addressed by operating the sensor at elevated temperature and/or through photo-assisted dissociation albeit at the cost of operational simplicity.

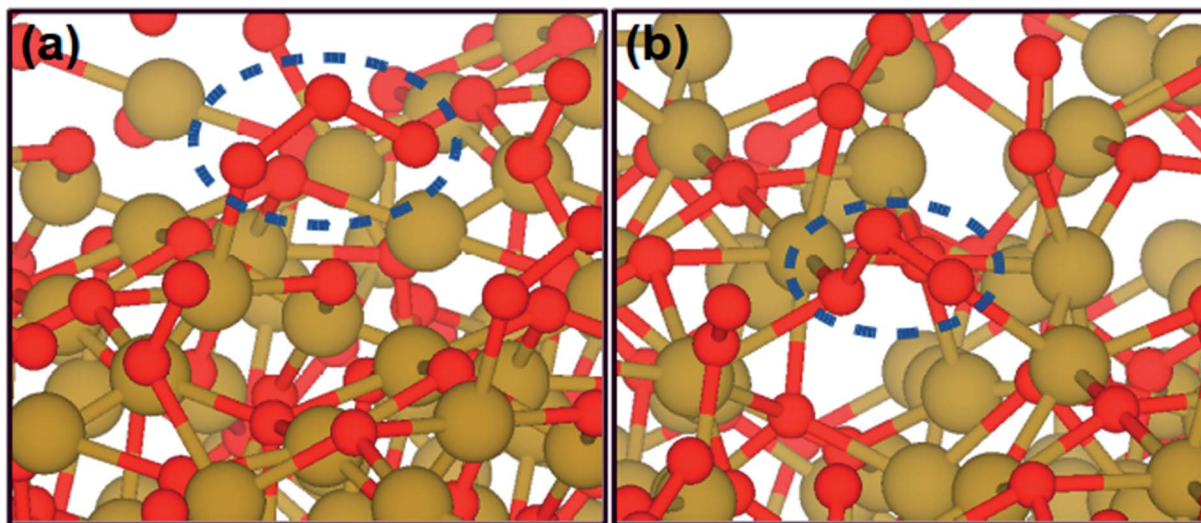


Fig. 7 Top views of  $\text{O}_3$  species over a (001)  $\text{Cu}_2\text{O}$  surface: (a) a chemisorbed  $\text{O}_3$  protrusion (dashed line) with one Cu–O bond. (b) An  $\text{O}_3$ -related bridge (dashed line) between surface Cu atoms. The  $\text{O}_3$  moiety forms three O–Cu bonds. (Cu: brown, O: red spheres).





## Conclusions

In summary, cuprous oxide nanocubes were successfully synthesized by a solution-based method at room temperature. When the Cu<sub>2</sub>O nanocubes were incorporated as the sensing element on IDEs, the resulting sensing element showed excellent sensitivity to O<sub>3</sub> in the range of 10 to 820 ppb, with fast response and recovery times. Importantly, the self-powered sensing elements of Cu<sub>2</sub>O nanocubes exhibited a high response (28%) at relatively low ozone concentration (10 ppb) with response and recovery times of 30 and 18 s, respectively. Finally, the p-type nature of the Cu<sub>2</sub>O nanocubes was confirmed, as the device current was found to increase in the presence of a strongly oxidizing gas, such as ozone.

## Conflicts of interest

There are no conflicts to declare.

## Acknowledgements

Current work was supported by COST Action TD1105 “EuNe-tAir” and by the EU FP7 Program (FP7-REGPOT-2012-2013-1) under grant agreement no. 316165. DFT calculations used computational resources provided by the Bibliotheca Alexandrina (see <http://hpc.bibalex.org>) and the GRNET HPC facility – ARIS – under projects AFOx and STEM. Part of this work was financially supported by the Stavros Niarchos Foundation within the framework of the project ARCHERS (“Advancing Young Researchers’ Human Capital in Cutting Edge Technologies in the Preservation of Cultural Heritage and the Tackling of Societal Challenges”). T. D. A. acknowledges financial support by the King Abdullah University of Science and Technology (KAUST).

## References

- W. H. O., “Air Quality Guidelines Global Update 2005. Particulate Matter, Ozone, Nitrogen Dioxide and Sulfur Dioxide,” Copenhagen, 2006.
- X. Wan, J. Wang, L. Zhu and J. Tang, *J. Mater. Chem. A*, 2014, **2**, 13641–13647.
- F. N. Meng, X. P. Di, H. W. Dong, Y. Zhang, C. L. Zhu, C. Li and Y. J. Chen, *Sens. Actuators, B*, 2013, **182**, 197–204.
- L. Wang, R. Zhang, T. Zhou, Z. Lou, J. Deng and T. Zhang, *Sens. Actuators, B*, 2016, **223**, 311–317.
- L. Wang, R. Zhang, T. Zhou, Z. Lou, J. Deng and T. Zhang, *Sens. Actuators, B*, 2017, **239**, 211–217.
- Y. Sui, Y. Zeng, W. Zheng, B. Liu, B. Zou and H. Yang, *Sens. Actuators, B*, 2012, **171–172**, 135–140.
- L. Gou and C. J. Murphy, *Nano Lett.*, 2003, **3**, 231–234.
- C. H. Kuo, C. H. Chen and M. H. Huang, *Adv. Funct. Mater.*, 2007, **17**, 3773–3780.
- S. Cao, T. Han, L. Peng, C. Zhao and J. Wang, *Ceram. Int.*, 2017, **43**, 4721–4724.
- Q. Cheng, W. Yan, L. Randeniya, F. Zhang and K. Ostrikov, *J. Appl. Phys.*, 2014, **115**, 12.
- J. Liu, S. Wang, Q. Wang and B. Geng, *Sens. Actuators, B*, 2009, **143**, 253–260.
- A. Labidi, H. Ouali, A. Bejaoui, T. Wood, C. Lambert-Mauriat, M. Maaref and K. Aguir, *Ceram. Int.*, 2014, **40**, 7851–7856.
- S. T. Shishiyani, T. S. Shishiyani and O. I. Lupan, *Sens. Actuators, B*, 2006, **1**, 468–476.
- A. R. Rastkar, A. R. Niknam and B. Shokri, *Thin Solid Films*, 2009, **517**, 5464–5467.
- T. A. P. Pattanasattayavong, S. Thomas, G. Adamopoulos and M. McLachlan, *Appl. Phys. Lett.*, 2013, **102**, 163505.
- X. J. N. Tang, B. Chen, Y. Xia and D. Chen, *RSC Adv.*, 2015, **5**, 54433–54438.
- H. Ouali, C. Lambert-Mauriat, L. Raymond and A. Labidi, *Appl. Surf. Sci.*, 2015, **351**, 840–845.
- S. Zhou, X. Fang, Z. Deng, D. Li, W. Dong, R. Tao, G. Meng and T. Wang, *Sens. Actuators, B*, 2009, **143**, 119–123.
- Z. Deng, X. Fang, D. Li, S. Zhou, R. Tao, W. Dong, T. Wang, G. Meng and X. Zhu, *J. Alloys Compd.*, 2009, **484**, 619–621.
- X. G. Zheng, K. Taniguchi, A. Takahashi, Y. Liu and C. N. Xu, *Appl. Phys. Lett.*, 2004, **85**, 1728–1729.
- S. Thirumalairajan, V. R. Mastelaro and C. A. Escanhoela, *ACS Appl. Mater. Interfaces*, 2014, 21739–21749.
- C. Baratto, R. Kumar, G. Faglia, K. Vojisavljević and B. Malić, *Sens. Actuators, B*, 2015, **209**, 287–296.
- S. Thirumalairajan and V. R. Mastelaro, *Sens. Actuators, B*, 2016, **223**, 138–148.
- P. Giannozzi, *J. Phys.: Condens. Matter*, 2009, **21**, 395502.
- D. J. G. Kresse, *Phys. Rev. B: Condens. Matter Mater. Phys.*, 1999, **59**, 1758–1775.
- C. F. P. Perdew, J. Chevary, S. Vosko, K. Jackson, M. Pederson and D. Singh, *Phys. Rev. B: Condens. Matter Mater. Phys.*, 1992, **46**, 6671–6687.
- S. Grimme, *J. Comput. Chem.*, 2006, **27**, 1787–1799.
- M. C. D. Chadi, *Phys. Rev. B: Condens. Matter Mater. Phys.*, 1973, **8**, 5747–5753.
- O. A. O. Jepsen, *Solid State Commun.*, 1971, **9**, 1763–1767.
- M. Valiev, E. J. Bylaska, N. Govind, K. Kowalski, T. P. Straatsma, H. J. J. Van Dam, D. Wang, J. Nieplocha, E. Apra, T. L. Windus and W. A. de Jong, *Comput. Phys. Commun.*, 2010, **181**, 1477–1489.
- H. A. S. Wilson, J. Bosco, Y. Tolstova, D. Scanlon and G. Watson, *Energy Environ. Sci.*, 2014, 3606–3610.
- A. D. Becke, *J. Chem. Phys.*, 1993, **98**, 5648–5652.
- L. I. Bendavid and E. A. Carter, *J. Phys. Chem. B*, 2013, **117**, 15750–15760.

